

Low-mass constraints on WIMP effective models of inelastic scattering using the Migdal effect

Sunghyun Kang,^a Stefano Scopel,^a Gaurav Tomar^b

^aDepartment of Physics, Sogang University, Seoul 121-742, South Korea

^bDepartment of Physics, Indian Institute of Technology Patna, Bihar-801106, India

E-mail: francis735@naver.com, scopel@sogang.ac.kr, tomar@iitp.ac.in

Abstract. We use the Migdal effect to extend to low masses the bounds on each of the effective couplings of the non-relativistic effective field theory of a WIMP of mass m_χ and spin 1/2 that interacts inelastically with nuclei by either upscattering to a heavier state with mass splitting $\delta > 0$ or by downscattering to a lighter state with $\delta < 0$. In order to do so we perform a systematic analysis of the Migdal bounds in the $m_\chi - \delta$ parameter space comparing them to those from nuclear recoil searches. The Migdal effect allows to significantly extend to low WIMP masses the nuclear recoil bounds for $\delta < 0$. In this case the bounds are driven by XENON1T, except when δ is vanishing or very small, when, depending on the WIMP–nucleus interaction, in the lower end of the m_χ range either DS50 or SuperCDMS are more constraining. On the other hand, when $\delta > 0$ and the WIMP particle upscatters to a heavier state nuclear recoil bounds are stronger than those from the Migdal effect.

Contents

1	Introduction	1
2	Inelastic Scattering of Dark Matter under the Migdal Effect	2
3	Analysis	5
4	Conclusion	13

1 Introduction

The absence of a signal from Weakly Interacting Massive Particles (WIMPs), the most popular dark matter (DM) candidates, has prompted the scientific community to optimize direct detection experiments to the search of sub-GeV DM [1–17]. One of the main challenges in detecting low-mass DM is the small energy deposited in the detector, which often lies below the detection thresholds. This makes it difficult to search for such DM particles, particularly through nuclear recoils. To overcome this challenge new analysis techniques such as the Migdal effect [18] have been put forward. The Migdal effect allows to detect low-mass DM through secondary atomic ionization, and occurs when the WIMP–nucleus scattering process triggers the emission of an electron from the target [15]. It has been pointed out that if the DM particle couples comparably to both protons and electrons, the Migdal ionization rate can dominate over electron scattering for certain DM masses and mediator types, particularly in the hundreds of MeV range [19, 20].

In direct detection experiments it is often easier to detect electromagnetic (EM) energy directly deposited in the measuring device compared to nuclear recoils, although it is more difficult to distinguish it from that generated from the background contamination. However, for very light WIMP masses the nuclear recoil process is kinematically not accessible, and the Migdal effect is the only way to detect a signal.

Recent studies [21, 22] have combined the Migdal effect with the Inelastic Dark Matter (IDM) scenario [23], where a WIMP state χ with mass m_χ interacts with nuclear targets by scattering to a different state χ' with mass $m_\chi + \delta$. The case $\delta < 0$, indicated in the literature as exothermic DM [24], implies the de-excitation of a meta-stable DM state that releases additional energy in the detector, allowing to extend further the sensitivity to very light WIMPs.

In Refs. [21] and [22] the Migdal effect for IDM was analyzed considering the cases of a spin-independent (SI) and spin-dependent (SD) WIMP–nucleus interaction, respectively. In our paper we wish to extend those analyses to a wider class of processes, by making use of the non-relativistic effective field theory (NREFT) framework [25, 26], that describes the most general WIMP–nucleus interactions for a particle of spin 1/2 by introducing a total of 14 momentum and velocity dependent operators (see Table 1). Since previous studies discuss only specific benchmark values of the IDM parameters we conduct a thorough scan in terms of δ and m_χ , showing that in absence of a signal the Migdal effect allows to exclude previously unexplored regions of the NREFT parameter space. In our analysis we employ the data from the XENON1T [27], DS50 [28], and SuperCDMS [29] experiments, revealing some degree of complementarity among them. The interplay between the

Migdal effect and elastic scattering has been previously explored within the NREFT framework in [10, 30].

Our paper is organized as follows: in Section 2 we summarize the Migdal effect within the context of IDM; our quantitative analysis is presented in Section 3; in Section 4 we provide our conclusions.

2 Inelastic Scattering of Dark Matter under the Migdal Effect

In this work we consider the inelastic scattering process $\chi T \rightarrow \chi' T$ of a DM particle χ off a nuclear target T . Due to energy conservation,

$$\frac{1}{2}\mu_{\chi T}v_T^2 = E_{\chi'} + E_T + \Delta, \quad (2.1)$$

where $\mu_{\chi T} = m_\chi m_T / (m_\chi + m_T)$ is the DM–nucleus reduced mass, $v_T \equiv |\vec{v}_T|$ is the DM particle incoming speed relative to the nucleus, that is assumed to be at rest in the lab rest frame. In the expression above $E_{\chi'}$ and E_T represent the energy of the outgoing DM particle and nucleus, respectively. Moreover, Δ is the amount of the initial kinetic energy of the DM particle lost due to the two simultaneous inelastic effects of the $\chi \rightarrow \chi'$ transition and the target ionization with the emission of one electron. In particular, it is expressed as $\Delta = E_{EM} + \delta$, where E_{EM} accounts for the electromagnetic energy deposited in the detector by the ionization process, and δ represents the mass splitting between the two DM states i.e. $\delta = m_{\chi'} - m_\chi$ ($\delta < 0$ corresponds to exothermic scattering and $\delta > 0$ to endothermic scattering, respectively). It is clear from Eq. (2.1) that the maximum value of Δ is equal to the initial available kinetic energy of the incoming WIMP,

$$\Delta_{\max} = \frac{1}{2}\mu_{\chi T}v_T^2. \quad (2.2)$$

The nuclear recoil energy in the frame of the detector is expressed as,

$$E_R = \frac{\mu_{\chi T}^2}{m_T}v^2 \left[1 - \frac{\Delta}{\mu_{\chi T}v^2} - \cos\theta \sqrt{1 - \frac{2\Delta}{\mu_{\chi T}v^2}} \right], \quad (2.3)$$

where θ is the DM–nucleon scattering angle in the center-of-mass frame. In Eq. (2.3), we made the approximation $\mu_{\chi' T} \simeq \mu_{\chi T}$.

In our analysis we focus on the electron ionization rate in Xe, Ar, and Ge targets, and make use of the ionization probabilities $p_{q_e}^c$ from [15], obtained under the single-atom approximation¹. In particular, the ionisation event rate in a direct detection experiment due to the Migdal effect is given by [15],

$$\frac{dR}{dE_{det}} = \int_0^\infty dE_R \int_{v_{min}(E_R)}^\infty dv_T \frac{d^3 R_{\chi T}}{dE_R dv_T dE_{det}}, \quad (2.4)$$

with

$$\frac{d^3 R_{\chi T}}{dE_R dv_T dE_{det}} = \frac{d^2 R_{\chi T}}{dE_R dv_T} \times \frac{1}{2\pi} \sum_{n,l} \frac{d}{dE_e} p_{q_e}^c(nl \rightarrow (E_e)). \quad (2.5)$$

¹Recently, the calculation of the ionization probabilities of [15] was improved using the Dirac-Hartree-Fock method [31]. In the ionization energy ranges relevant to our analysis both calculations lead to similar results.

In our analysis we include the electrons up to the shells, $n = 3, 4, 5$. It is worth noticing that in the lab frame the ionization probabilities p_{qe}^c are boosted due to the recoil of the nucleus, and scale linearly with E_R [15]. The Migdal effect is only relevant at low WIMP masses and becomes subdominant as soon as nuclear recoils are kinematically allowed. In the expression above E_{det} represents the total deposited energy and is given by,

$$\begin{aligned} E_{det} &= QE_R + E_{EM} + \delta = QE_R + \Delta, \\ E_{EM} &= E_e + E_{nl}, \end{aligned} \quad (2.6)$$

where Q is the quenching factor, E_e represents the energy of the outgoing electron and E_{nl} the atomic de-excitation energy. In particular for $\Delta \leq 0$ the electromagnetic energy QE_R produced by the recoil of the nucleus is always negligible compared to that produced by the Migdal process, leading to $E_{det} \simeq E_{EM} + \delta$. The minimum and the maximum of the recoil energy E_R are obtained from Eq. (2.3), using $\theta = 0$ and π respectively. Finally, the minimum DM velocity required for the recoil of the nucleus at a given energy E_R is given by,

$$v_{min}(E_R) = \frac{1}{\mu_{\chi T} \sqrt{2m_T E_R}} |m_T E_R + \mu_{\chi T} \Delta|. \quad (2.7)$$

In our analysis, we adopt a standard Maxwell–Boltzmann velocity distribution at rest in the Galactic frame with escape velocity $v_{esc} = 550$ km/s and boosted to the solar rest frame with rotation speed of $v_0 = 220$ km/s.

As a result of the small momentum transfer the WIMP–nucleus scattering process is non relativistic and can be described in terms of the most general NREFT allowed by symmetry under Galilean boosts [25, 26]. In this context, the expression for the interaction Hamiltonian between the target nucleus, and the WIMP particle is given by,

$$\mathcal{H}(\mathbf{r}) = \sum_{\tau=0,1} \sum_{j=1}^{15} c_j^\tau \mathcal{O}_j(\mathbf{r}) t^\tau, \quad (2.8)$$

with $t^0 = 1$ and $t^1 = \tau_3$ the 2×2 identity and third Pauli matrix in isospin space, respectively. The isoscalar and isovector (dimension -2) coupling constants c_j^0 and c_j^1 , are related to those to protons and neutrons c_j^p and c_j^n by $c_j^p = (c_j^0 + c_j^1)/2$ and $c_j^n = (c_j^0 - c_j^1)/2$. For a spin-1/2 WIMP there are 14 operators \mathcal{O}_j [25, 26, 32], which depend at most linearly on the transverse velocity v^\perp (defined as the component of \vec{v}_T perpendicular to the transferred momentum \vec{q}), and that are listed in Table 1. In the case of the standard SI and SD interactions (corresponding to the \mathcal{O}_1 and \mathcal{O}_4 operators, respectively, in the convention of [25, 26]) it is common to express the couplings c_1^N and c_4^N (with $N = p, n$) in terms of the corresponding WIMP–nucleon scattering cross-sections,

$$\begin{aligned} \sigma_{SI}^N &= \frac{(c_1^N)^2 \mu_{\chi N}^2}{\pi}, \\ \sigma_{SD}^N &= \frac{3}{16} \frac{(c_4^N)^2 \mu_{\chi N}^2}{\pi}, \end{aligned} \quad (2.9)$$

where $\mu_{\chi N}$ is the WIMP–nucleon reduced mass.

$\mathcal{O}_1 = 1_\chi 1_N$	$\mathcal{O}_9 = i\vec{S}_\chi \cdot (\vec{S}_N \times \frac{\vec{q}}{m_N})$
$\mathcal{O}_3 = i\vec{S}_N \cdot (\frac{\vec{q}}{m_N} \times \vec{v}^\perp)$	$\mathcal{O}_{10} = i\vec{S}_N \cdot \frac{\vec{q}}{m_N}$
$\mathcal{O}_4 = \vec{S}_\chi \cdot \vec{S}_N$	$\mathcal{O}_{11} = i\vec{S}_\chi \cdot \frac{\vec{q}}{m_N}$
$\mathcal{O}_5 = i\vec{S}_\chi \cdot (\frac{\vec{q}}{m_N} \times \vec{v}^\perp)$	$\mathcal{O}_{12} = \vec{S}_\chi \cdot (\vec{S}_N \times \vec{v}^\perp)$
$\mathcal{O}_6 = (\vec{S}_\chi \cdot \frac{\vec{q}}{m_N})(\vec{S}_N \cdot \frac{\vec{q}}{m_N})$	$\mathcal{O}_{13} = i(\vec{S}_\chi \cdot \vec{v}^\perp)(\vec{S}_N \cdot \frac{\vec{q}}{m_N})$
$\mathcal{O}_7 = \vec{S}_N \cdot \vec{v}^\perp$	$\mathcal{O}_{14} = i(\vec{S}_\chi \cdot \frac{\vec{q}}{m_N})(\vec{S}_N \cdot \vec{v}^\perp)$
$\mathcal{O}_8 = \vec{S}_\chi \cdot \vec{v}^\perp$	$\mathcal{O}_{15} = -(\vec{S}_\chi \cdot \frac{\vec{q}}{m_N})((\vec{S}_N \times \vec{v}^\perp) \cdot \frac{\vec{q}}{m_N})$

Table 1: Non-relativistic Galilean invariant operators for dark matter with spin 1/2.

The detailed expression for the calculation of the differential rate $\frac{d^2 R_{\chi T}}{dE_R dv_T}$ in Eq. (2.5) is provided in Section 2 of [33], which has been implemented in the WimPyDD code [34]. In particular, in the non-relativistic limit the WIMP–nucleus differential cross section is proportional to the squared amplitude,

$$\frac{d\sigma_T}{dE_R} = \frac{2m_T}{4\pi v_T^2} \left[\frac{1}{2j_\chi + 1} \frac{1}{2j_T + 1} |\mathcal{M}_T|^2 \right], \quad (2.10)$$

with m_T the nuclear mass, j_T, j_χ the spins of the target nucleus and of the WIMP, where $j_\chi = 1/2$, and [26],

$$\frac{1}{2j_\chi + 1} \frac{1}{2j_T + 1} |\mathcal{M}_T|^2 = \frac{4\pi}{2j_T + 1} \sum_{\tau=0,1} \sum_{\tau'=0,1} \sum_k R_k^{\tau\tau'} \left[c_i^\tau, c_j^{\tau'}, (v^\perp)^2, \frac{q^2}{m_N^2} \right] W_{Tk}^{\tau\tau'}(y). \quad (2.11)$$

In the expression above the squared amplitude $|\mathcal{M}_T|^2$ is summed over initial and final spins and the $R_k^{\tau\tau'}$'s are WIMP response functions provided, for instance, in Eq. (38) of [26]. They depend on the couplings c_j^τ as well as the transferred momentum, while,

$$(v^\perp)^2 = v_T^2 - v_{min}^2, \quad (2.12)$$

and v_{min} is given by Eq. (2.7). Moreover, in Eq. (2.11) the $W_{Tk}^{\tau\tau'}(y)$'s are nuclear response functions and the index k represents different effective nuclear operators, which, under the assumption that the nuclear ground state is an approximate eigenstate of P and CP , can be at most eight: following the notation in [25, 26], $k=M, \Phi'', \Phi''M, \Phi', \Sigma'', \Sigma', \Delta, \Delta\Sigma'$. The $W_{Tk}^{\tau\tau'}(y)$'s are function of $y \equiv (qb/2)^2$, where b is the size of the nucleus. For the target nuclei T used in most direct detection experiments the functions $W_{Tk}^{\tau\tau'}(y)$, calculated using nuclear shell models, have been provided in Refs. [26, 35].

The ionization probabilities p_{qe}^c are calculated using the impulse approximation, that assumes that the DM–nucleus collisions happen rapidly compared to the time scale set by the potential well of the detector lattice, $1/\omega_{ph}$, with ω_{ph} the phonon frequency [36]. In particular, the time scale of DM–nucleus collision and the emission of Migdal electrons is of the order $t \simeq 1/E_R$ (in natural units). As a consequence, the validity of the impulse approximation implies a lower cut on E_R .

In the case of a xenon fluid, we utilise a time scale of $t = 10^{-12}$ s, which applies to xenon at 170K [21]. Consequently, in the energy integration of Eq. (2.4) we set $E_R > E_{cut} = 100t^{-1} \approx 50$ meV. Using Eq. (2.3) for elastic scattering this implies $m_\chi \geq 0.02$ GeV. However, through the Δ parameter the lower bound on m_χ depends on the mass splitting δ and on the experimental threshold on E_{det} . For instance, taking into account the XENON1T energy threshold (see Section 3) for $\delta = -10$ keV, one gets $m_\chi \geq 0.6$ MeV.

For an argon fluid at 90K using an inter-atomic distance of 4 angstroms and a sound speed of 847.55 m/s [37], we estimate a time scale of $t = a/v_s \approx 10^{-12}$ s leading again to $E_{cut} \simeq 50$ meV. In the case of elastic scattering, this implies $m_\chi \geq 0.01$ GeV. For $\delta = -10$ keV, we set $m_\chi \geq 0.2$ MeV.

As far as the germanium target is concerned, we closely follow the work of [36], where it is shown that the impulse approximation holds if the momentum transfer q_T satisfies the condition $q_T \geq \sqrt{2m_T\omega_{ph}}$, with ω_{ph} estimated between 30–50 meV for a typical crystal. Taking a conservative approach, we assume $E_{cut} = 50$ meV. Using this criterion, we find $m_\chi \geq 0.016$ GeV for elastic scattering, while for $\delta = -10$ keV, we obtain $m_\chi \geq 0.34$ MeV.

In the case of endothermic scattering ($\delta > 0$) rather than from the impulse approximation cut the lower bound on m_χ is obtained from kinematics, specifically from the requirement that the argument of the square root in Eq. (2.3) is positive. For instance, for $\delta = 10$ keV this leads to $m_\chi \gtrsim 3$ GeV (independent on the target as long as $m_\chi \ll m_T$).

3 Analysis

The Migdal event rate is obtained by multiplying the WIMP–nucleus scattering rate $\frac{d^2 R_{\chi T}}{dE_R dv_T}$ with the ionization probability p_{qe}^c (Eq. (2.5)). As shown in Eq. (2.7), the emission of an electron leads to modifications in the kinematics of the scattering rate R compared to elastic scattering. In particular, Eq. (2.7) mimics that for the kinematics of IDM [23], with the replacement of the mass splitting δ with Δ , defined as $\Delta = E_{EM} + \delta$.

In WimPyDD [34] we implement the kinematics of the Migdal effect through the argument `delta` of the `wimp_dd_rate` routine. Specifically, we adopted `delta = E_{EM} + \delta \simeq E_e + \delta, and integrated the scattering rate over the undetected nuclear scattering energy $E_R > E_{cut} \simeq 50$ meV, in order to comply with the impulse approximation as discussed in the previous Section. Furthermore, we used the ionization probability p_{qe}^c for Xe, Ar, and Ge atoms from [15], corresponding to the XENON1T [27], DS50 [28], and SuperCDMS [29] experiments, respectively.`

In Fig. 1 we provide an explicit example of the energy dependence of the Migdal differential rate in the case of different NREFT interactions, for a Xe target and $m_\chi = 0.5$ GeV. In all the plots the curves have the same normalization, to show that the NREFT interaction has a mild effect on the energy spectrum, which is mainly determined by the nuclear ionization probabilities. The solid red, dashed blue, and dotted green lines represent $\delta = -10$ keV (exothermic), $\delta = 0$ keV, and $\delta = 1$ keV (endothermic), respectively, for all the 14 interaction couplings of Eq. (2.8). Different peaks in Fig. 1 correspond to the contributions of the shells $n = 3, 4, 5$. It is worth mentioning that depending on the thresholds of the considered experiments, only some of the shells contribute to the Migdal event rate.

To calculate our constraints, for XENON1T we use the analysis of Ref. [27] adopting the single energy bin $0.186 \text{ keV} \leq E_{det} \leq 3.8 \text{ keV}$ and an exposure of 22 tonne-days. In particular, in [27] 61

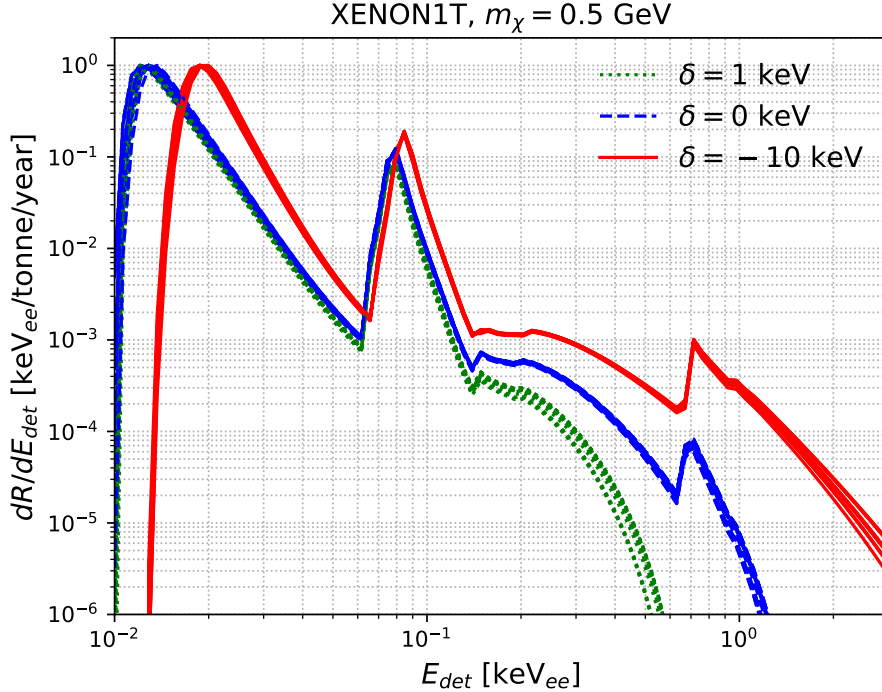


Figure 1: The normalized Migdal spectrum is obtained from DM scattering with the xenon target for $m_\chi = 0.5$ GeV, considering $\delta = 1, 0$, and -10 keV, incorporating all the NREFT interactions. Similar conclusions apply to argon and germanium targets.

events were observed, with an expected background of 23.4 events, yielding a 90% C.L. constraint of 49 events.

The SuperCDMS collaboration recently conducted a dedicated Migdal analysis [29]. They examined two datasets with exposures of 18.8 kg-days and 17.5 kg-days. For both datasets we consider the single energy bin $0.07 \text{ keV} \leq E_{det} \leq 2 \text{ keV}$ with 208 and 193 DM events [38], respectively, and use the energy resolution and efficiency from [38]. Among the two datasets in our plots we present the most constraining one.

As observed in [30], the analysis of DS50 [28] relies on a profile-likelihood procedure which is difficult to reproduce. However, as already pointed out, the shape of the Migdal energy spectrum measured experimentally is fixed by the ionisation probabilities and is approximately the same for all WIMP-nucleon interactions, which only determine the overall normalization. As a result we can use the normalisation of the exclusion plot in [28], valid for a standard SI interaction, to obtain the bounds for all the other interaction operators in Eq. (2.8) by a simple rescaling with the total number of events predicted for each interaction. In particular, to reproduce the exclusion Migdal limit of Fig. 3 in [28] we adopt the energy bin $0.083 \text{ keV} \leq E_{EM} \leq 0.106 \text{ keV}$ with 20 events, and an exposure of $\simeq 12.5$ tonne-day.

In Fig. 2 we plot the nuclear recoil spectrum for a Xe target, taking $m_\chi = 1$ GeV. From such plot one can observe that for endothermic DM ($\delta > 0$) the normalization of the spectrum

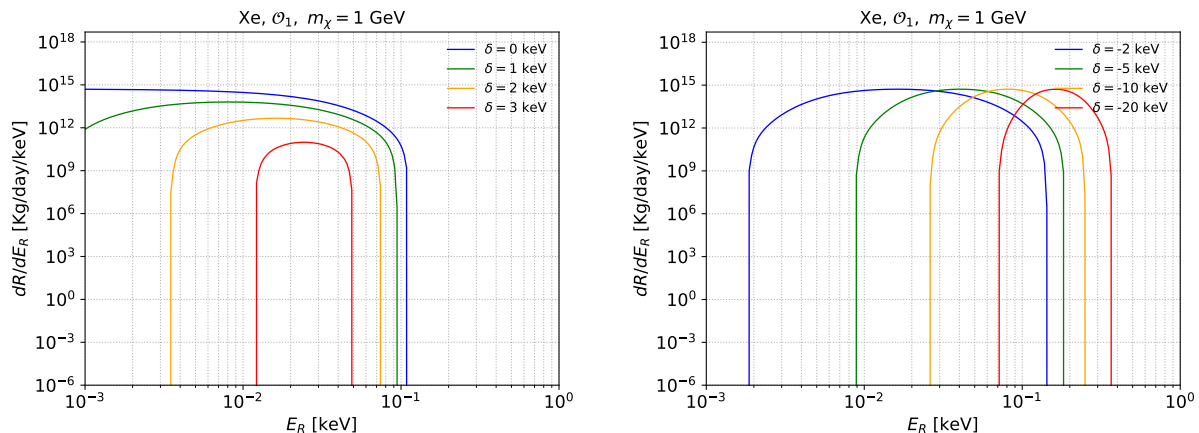


Figure 2: The nuclear recoil spectrum for $\delta < 0$ (exothermic), $\delta = 0$, and $\delta > 0$ (endothermic) scattering of DM with a Xe target is considered, assuming \mathcal{O}_1 interaction with a DM mass of $m_\chi = 1$ GeV.

decreases with δ while at the same time the energy interval where the spectrum is different from zero shrinks. This leads to a suppression of the Migdal signal. On the other hand for exothermic scattering ($\delta < 0$) both the minimum and the maximum nuclear recoil energies are shifted to higher values for growing $|\delta|$, while the normalization of the spectrum remains the same. This leads to an enhancement for the Migdal signal because, as previously pointed out, the ionization probabilities grow linearly with E_R due to the boost from the recoiling atom to the lab frame. Similar conclusions hold for other NREFT interactions and targets, so that, on general grounds, compared to the elastic case the Migdal signal is enhanced for $\delta < 0$ and suppressed for $\delta > 0$. It is again important to mention that the shape of the Migdal energy spectrum is determined by the ionization probabilities p_{qe}^c and remains approximately the same irrespective of the interaction operator, of m_χ and of δ .

The results of our analysis are presented in Figs. 3–12. In all our plots we assume one non-vanishing coupling at a time in the effective Hamiltonian of Eq. (2.8) and an isoscalar interaction, i.e. $c_j^1 = 0$. In Figs. 3–5 the exclusion limits on each effective coupling c_j are shown as a function of m_χ for $\delta = 0$, while in Fig. 6–8 we show the analogous results for $\delta = -10$ keV. The exclusion limit on the same couplings are explored in the $m_\chi - \delta$ plane in Figs. 9–11. Additionally, the constraints on the standard SI and SD cross-sections (Eq. 2.9) in the $m_\chi - \delta$ plane are presented in Fig. 12. In particular, from Figs. 9–11, it is evident that the Migdal exclusion bounds are overcome by those from nuclear recoil for $\delta \gtrsim 3$ keV. For this reason in Figs. 3–8 we have only shown exclusion limits for $\delta = 0$ and $\delta < 0$, omitting $\delta > 0$.

In Figs. 3–8, the Migdal exclusion limits from XENON1T, SuperCDMS, and DS50 experiments are represented by blue-dashed, cyan-dashed, and green-dashed lines, respectively. The shaded grey region in each plot represents the area excluded by nuclear recoil obtained from the data of a variety of experiments, including XENON1T [39], PICO60 (using a C_3F_8 [40] and a CF_3I target [41]), DS50 [42], LZ [43], CDEX [44], CDMSLite [45], COSINE [46], COUPP [47], CRESST-II [48], PANDAX-II [49], PICASSO [50], SuperCDMS [51], and XENONnT [52]. From these experiments we select the most constraining bound for each combination of m_χ and δ .

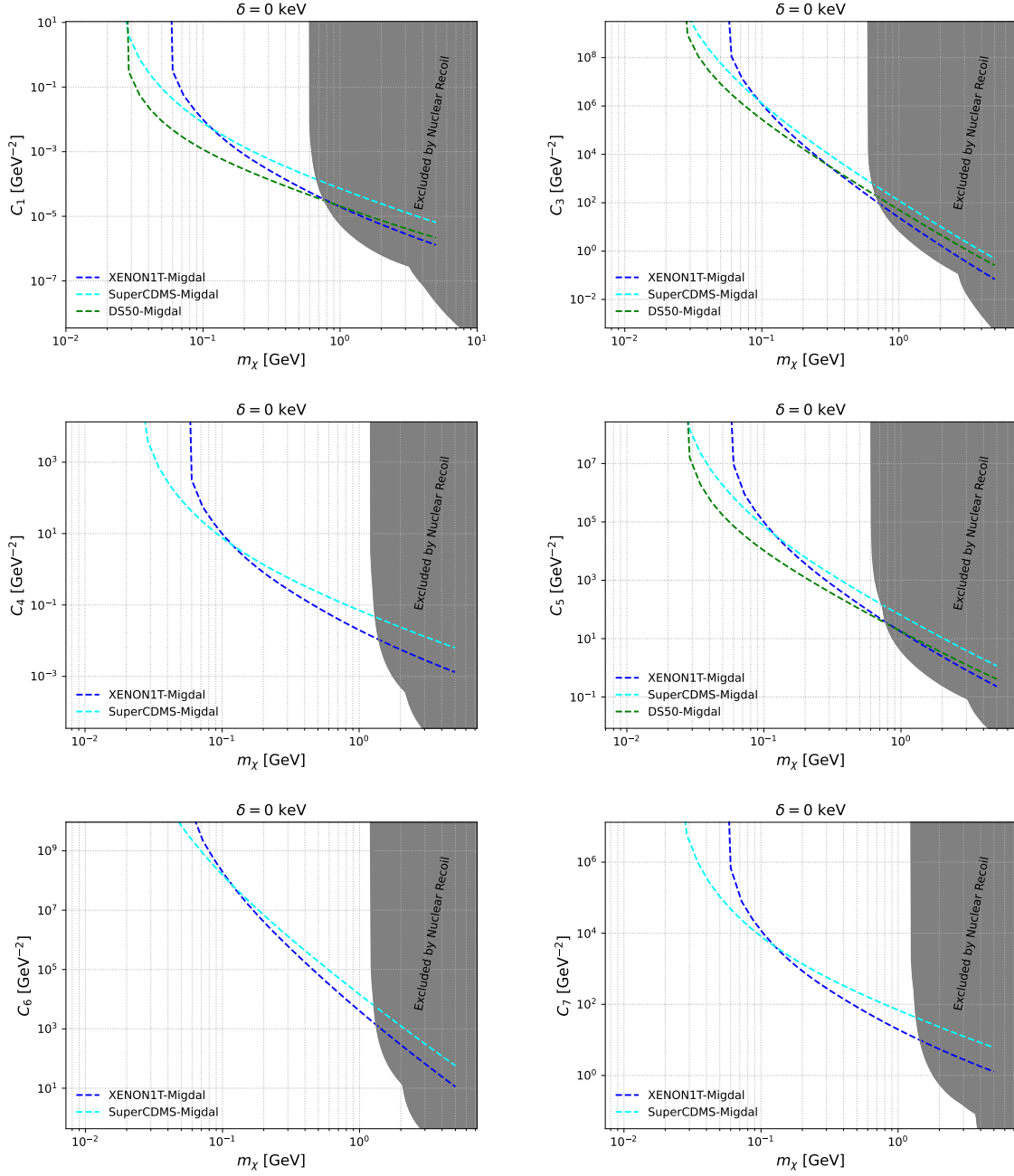


Figure 3: Migdal exclusion limit for the XENON1T (blue-dashed), SuperCDMS (cyan-dashed), and DS50 (green-dashed) experiments and for the $O_{1,3,4-7}$ interactions, considering elastic scattering, $\delta = 0$ keV. The grey shaded region represents the combined exclusion limit from experiments searching for nucleus scattering events.

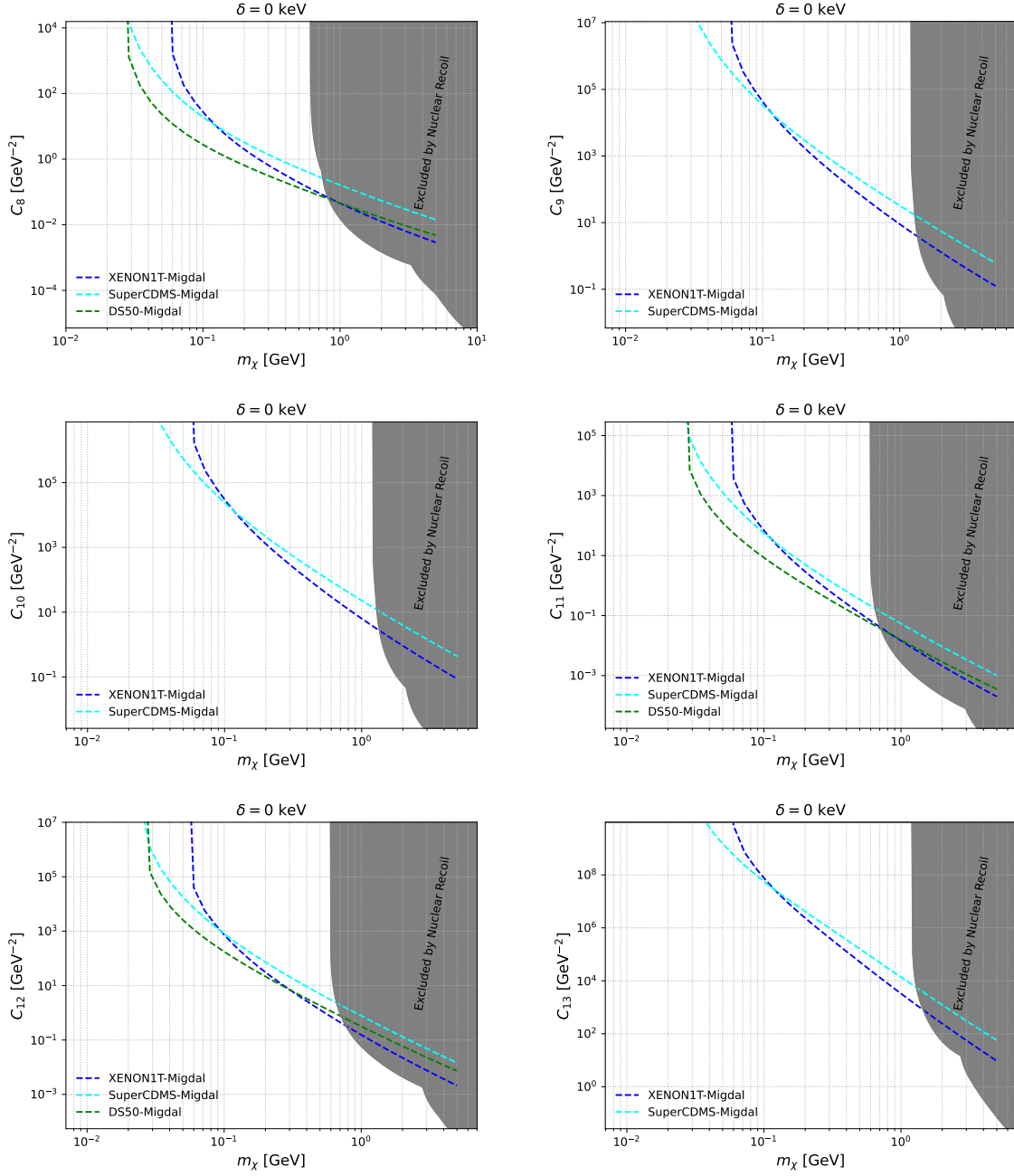


Figure 4: Same as Fig. 3 for the $\mathcal{O}_{8,9,10-13}$ interactions.

In Figs. 3–11 we separate the interaction operators \mathcal{O}_j among SI-type and SD-type. The SI-type operators (\mathcal{O}_1 , \mathcal{O}_3 , \mathcal{O}_{11} , \mathcal{O}_{12} and \mathcal{O}_{15}) are enhanced for heavy targets and are driven either by the $W_{TM}^{\tau\tau'}$ or by the $W_{T\Phi''}^{\tau\tau'}$ nuclear response functions (see Eq. (2.11)). In particular

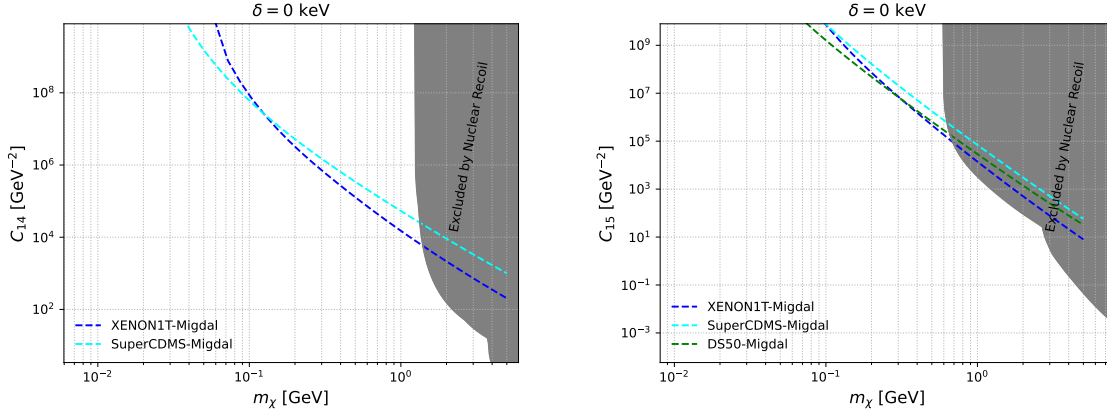


Figure 5: Same as Fig. 3 for O_{14} and O_{15} interactions.

$W_{TM}^{\tau\tau'}$ corresponds to the standard SI coupling, proportional to the square of the nuclear mass number; on the other hand, $W_{T\Phi}^{\tau\tau'}$ is non vanishing for all nuclei and favors heavier elements with large nuclear shell orbitals not fully occupied. The SD interactions ($O_4, O_6, O_7, O_9, O_{10}, O_{13}, O_{14}$) vanish when the spin of the nucleus is zero. Among them O_4, O_6, O_7, O_9 and O_{10} , O_{14} couple to $W_{T\Sigma}^{\tau\tau'}$ and $W_{T\Sigma''}^{\tau\tau'}$ which are driven by the spin of the target (the sum $W_{T\Sigma}^{\tau\tau'} + W_{T\Sigma''}^{\tau\tau'}$ corresponds to the standard spin-dependent form factor). The O_{13} operator couples to the $W_{T\Phi}^{\tau\tau'}$, which requires a target spin $j_T > 1/2$. Finally, the two operators O_5 and O_8 deserve a separate discussion, since, at variance with all other cases, for them velocity-suppressed contributions (proportional to $(v^\perp/c)^2 \simeq \mathcal{O}(10^{-6})$) can be of the same order of velocity-independent ones. As a consequence they are driven by a combination of $W_{T\Delta}^{\tau\tau'}$ (that is velocity-independent and couples to the nuclear spin) and $W_{TM}^{\tau\tau'}$ (velocity suppressed). In particular, in Ar, that has no spin, $W_{T\Delta}^{\tau\tau'}$ vanishes and the signal is driven by $W_{TM}^{\tau\tau'}$, so it is of the SI-type. On the other hand, in the case of Ge and Xe both $W_{T\Delta}^{\tau\tau'}$ and $W_{TM}^{\tau\tau'}$ are different from zero: for Ge $W_{T\Delta}^{\tau\tau'}$ drives the signal, since the contribution of $W_{TM}^{\tau\tau'}$ is negligible due to the velocity suppression, so it can be considered of the SD-type; on the other hand in Xe the enhancement of $W_{TM}^{\tau\tau'}$ due to the large target mass compensates for the velocity suppression, so that it can be considered of the SI-type. From Figs. 3–5 one can see that for $\delta = 0$ the Migdal effect allows to probe (exclude) $m_\chi \gtrsim 30$ MeV, while nuclear recoil reaches $m_\chi \gtrsim 600$ MeV for SI-type interactions and $m_\chi \gtrsim 1$ GeV for SD ones. For $\delta = 0$ similar conclusions were drawn within the framework of a relativistic effective field theory in [30], although in such scenario only a subset of the 14 NR operators O_j considered here contributes to scattering process at low energy. So the present study complements [30] by exploring the missing operators. The use of the Migdal effect allows to significantly extend the sensitivity of direct detection searches to lower WIMP masses also thanks to the complementarity of different experiments. In particular in Figs. 3–5 for SI-type interactions DS50 [28] determines the bounds for $m_\chi \gtrsim 30$ MeV and XENON1T [27] at higher m_χ . On the other hand, since the Ar target has no spin DS50 does not put any bound on SD-type interactions, where, instead, the bounds are driven by SuperCDMS [29] at low WIMP mass due to its low 70 eV threshold, while XENON1T [27] overcomes the SuperCDMS exclusion

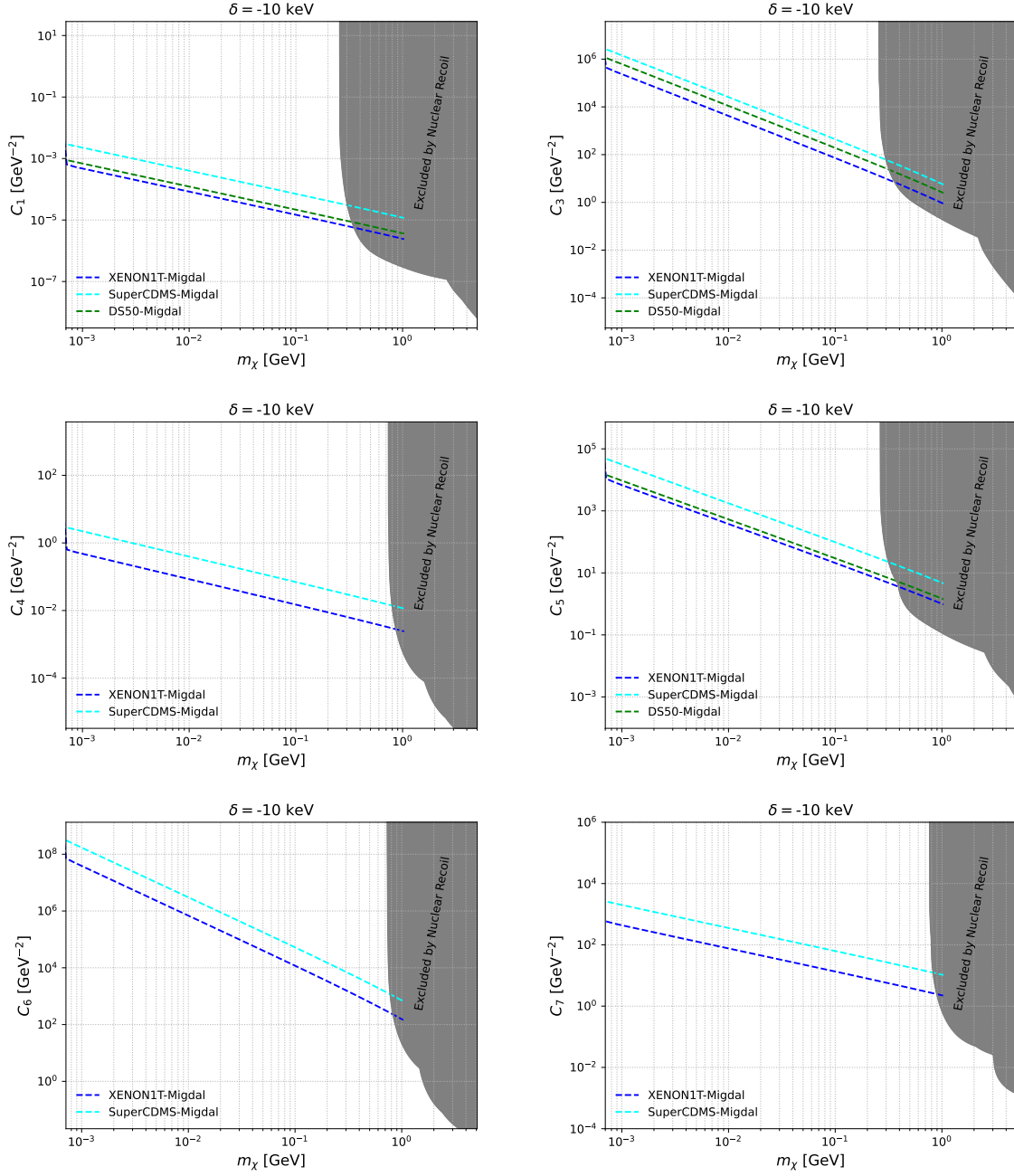


Figure 6: Migdal exclusion limit for XENON1T (blue), SuperCDMS (cyan), and DS50 (green) experiments for $O_{1,3,4-7}$ interactions, considering exothermic scattering, $\delta = -10$ keV. Combined exclusion limit from exothermic DM–nucleus scattering in direct detection experiments is presented as a grey shaded region.

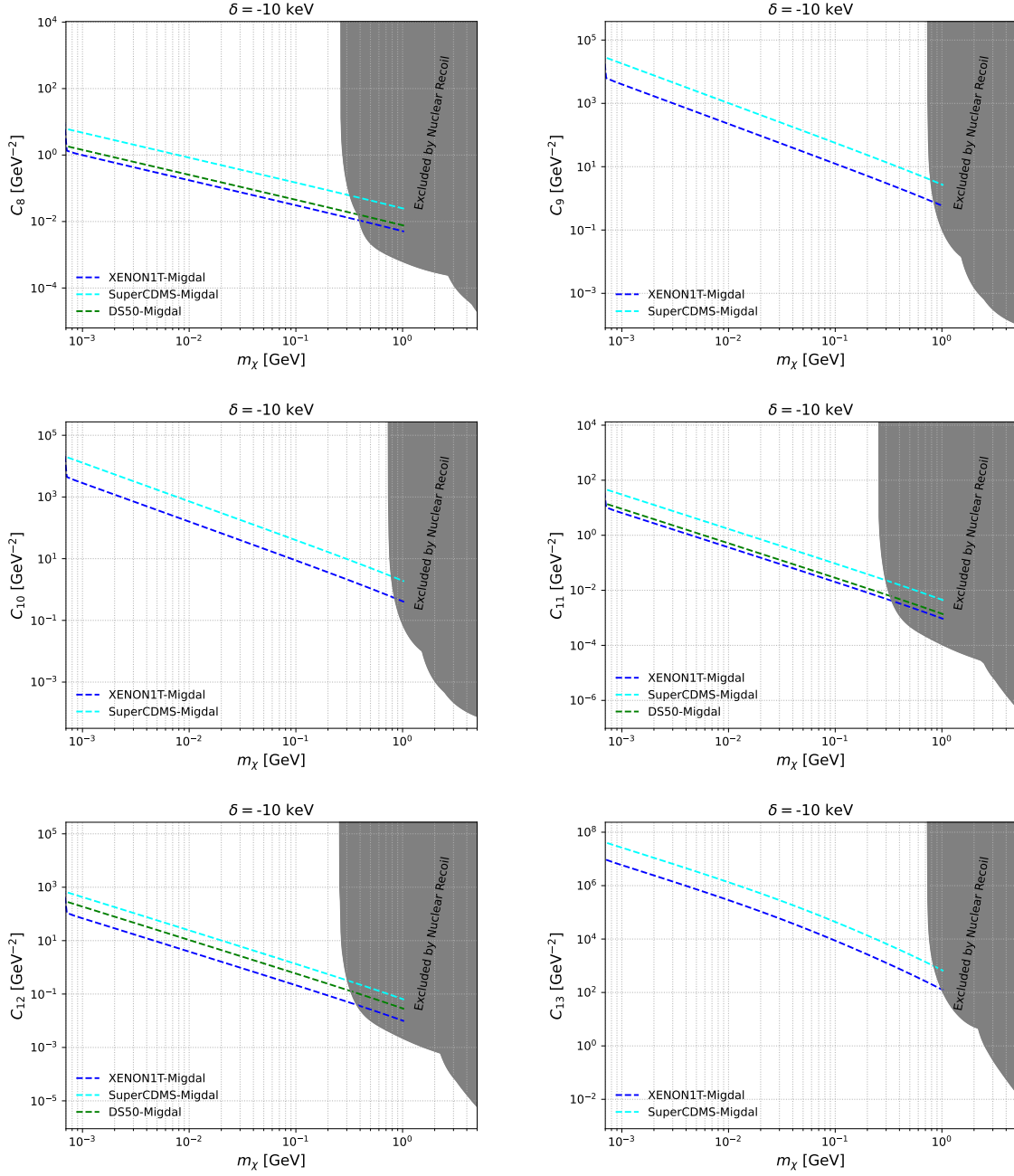


Figure 7: Same as Fig. 6 for $O_{8,9,10-13}$ interactions

limit for $m_\chi \geq 100$ MeV.

The exclusion limits for the exothermic scattering are presented for $\delta = -10$ keV in Figs. 6–8. In this scenario XENON1T drives all the bounds which, compared to the case $\delta = 0$, become flat at

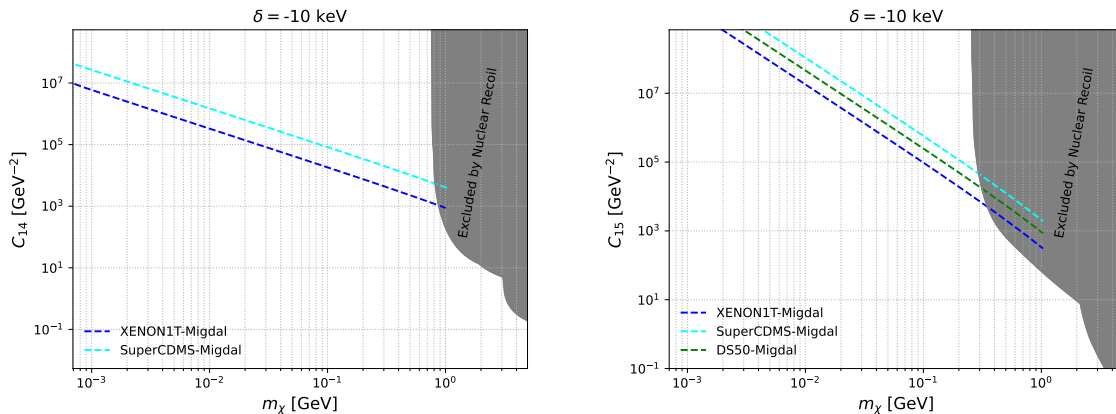


Figure 8: Same as Fig. 6 for O_{14} and O_{15} interactions

low WIMP masses and saturate the lower cut on the WIMP mass discussed in Section 2 required to comply with the impulse approximation.

Figs. 9–11 show the bounds on the c_j effective couplings in the $m_\chi - \delta$ plane. The contours show the most constraining bound among XENON1T [27], DS50 [28], and SuperCDMS [29]. As in the previous plots the shaded grey regions show the areas excluded by nuclear recoil searches. The dashed green, cyan, and blue lines correspond to the impulse approximation cut $E_R^{max} \geq 50$ meV for Ar, Ge, and Xe respectively, showing that the latter determines the upper edges of the contour plots. In this regime the signal is suppressed and eventually vanishes, so such boundaries represents an approximation of the maximal reach of Migdal searches. Their accurate determination would require to calculate the Migdal expected rate beyond the impulse approximation.

4 Conclusion

In the present paper we have used the Migdal effect to obtain constraints on the Inelastic Dark Matter scenario at low WIMP mass within the NREFT framework. In order to do so we have included the experimental results from XENON1T, SuperCDMS, and DS50. To calculate the bounds we have assumed one non-vanishing coupling at a time in the effective Hamiltonian of Eq. (2.8) and an isoscalar interaction, i.e. $c_j^1 = 0$.

The result of our analysis is that the use of the Migdal effect allows to significantly extend the sensitivity of direct detection searches to lower WIMP masses, especially for exothermic dark matter, $\delta < 0$. In particular, the bounds are driven by XENON1T with the exceptions of the case of a vanishing or very small mass splitting δ . In this case DS50 drives the bound when $m_\chi \leq 0.7$ GeV and the interaction is of the SI-type, while SuperCDMS determines the bound for $m_\chi \leq 0.1$ GeV and the interaction is of the SD-type. On the other hand, when $\delta \gtrsim 0$ the sensitivity of standard direct detection experiments that measure the recoil energy of the nucleus exceeds that of experiments searching for the Migdal effect.

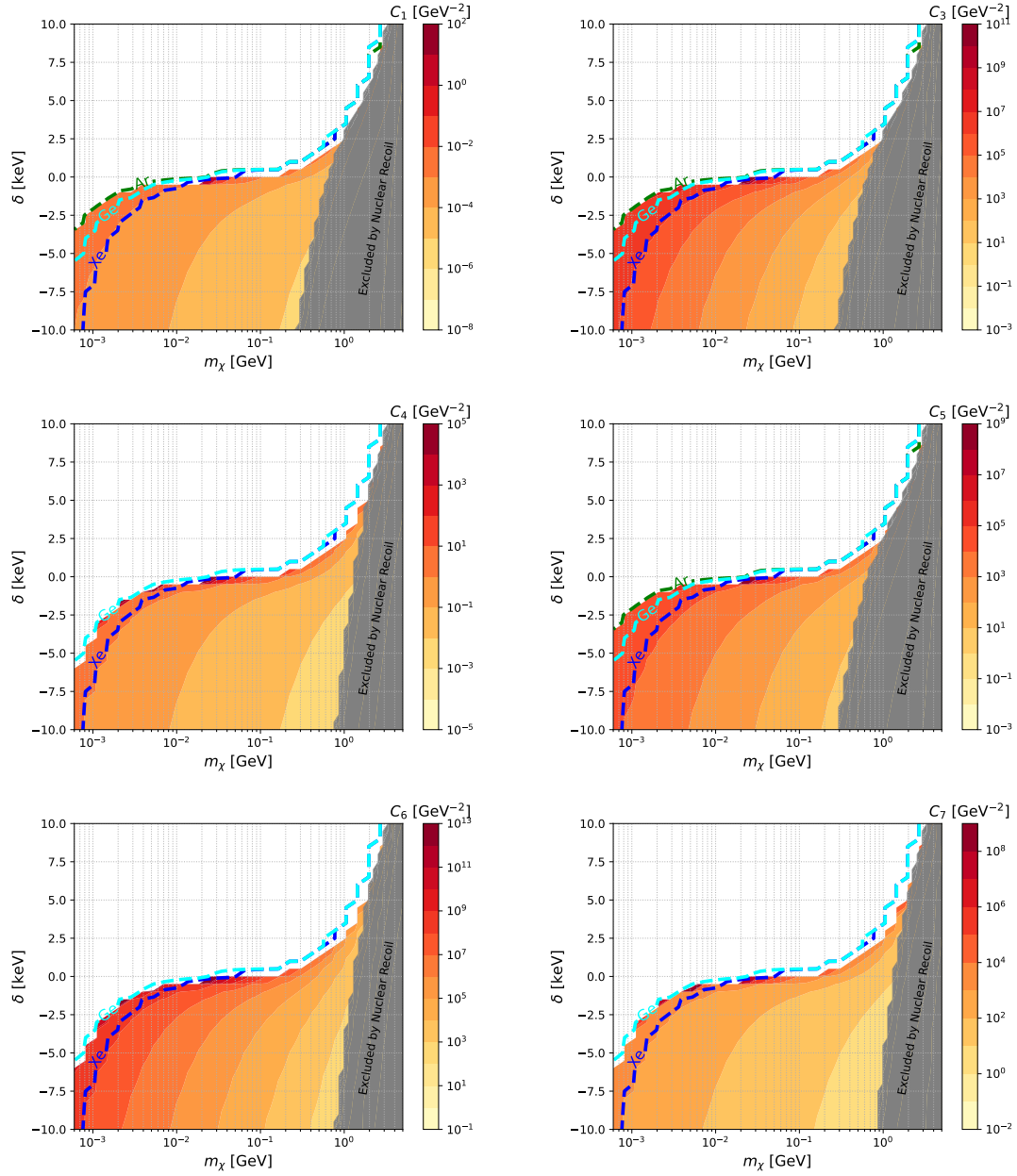


Figure 9: Combined exclusion plots for $O_{1,2,3-7}$ interactions are presented in the $m_\chi - \delta$ plane. The color gradient delineates regions excluded by Migdal data from XENON1T, SuperCDMS, and DS50 experiments, while the shaded grey region represents data from direct detection experiments included in our analysis. Additionally, dashed lines in green, cyan, and blue denote $E_R^{max} < 50$ meV for Ar, Ge, and Xe targets, respectively, obtained through the impulse approximation.

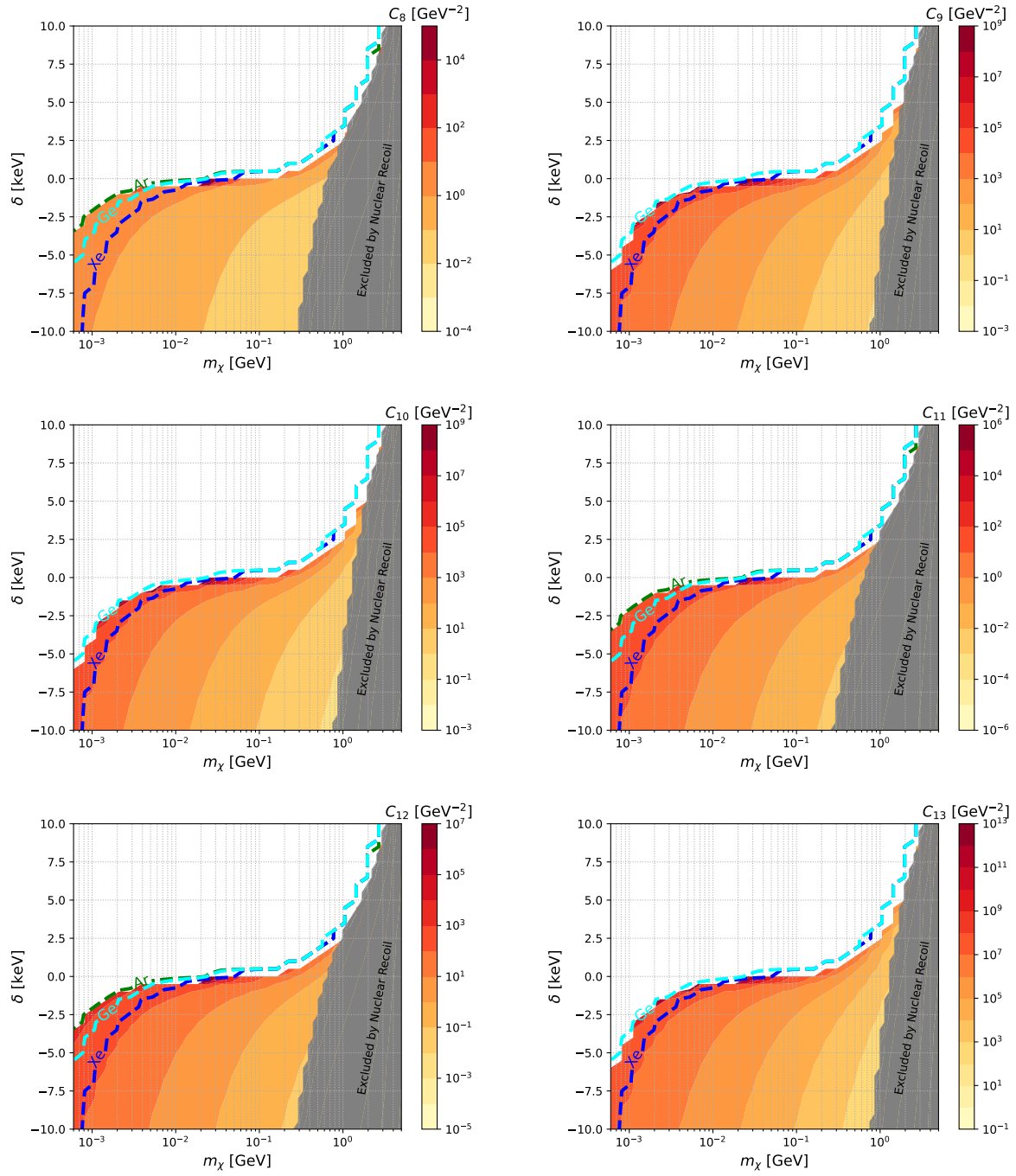


Figure 10: Same as Fig. 9 for $O_{8,9,10-13}$ interactions.

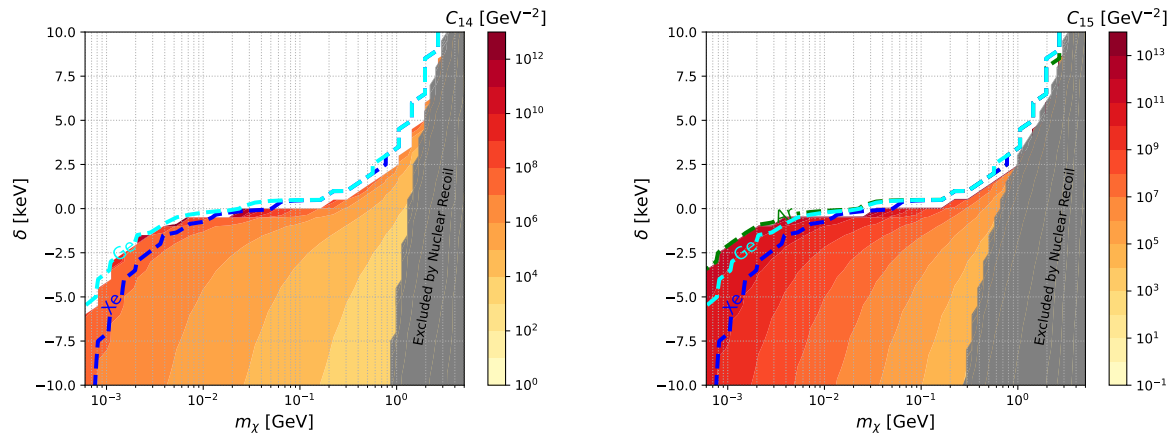


Figure 11: Same as Fig. 9 for O_{14} and O_{15} interactions.

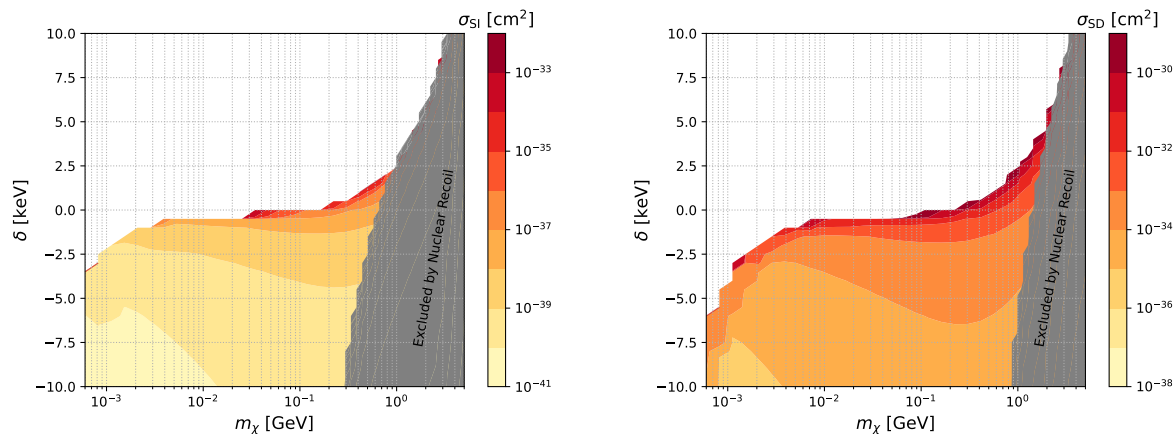


Figure 12: Combined exclusion limits for SI and SD interaction in the $m_\chi - \delta$ plane.

Acknowledgments

The work of S.K. and S.S. is supported by the National Research Foundation of Korea (NRF) funded by the Ministry of Education through the Center for Quantum Space Time (CQUeST) with grant number 2020R1A6A1A03047877 and by the Ministry of Science and ICT with grant number RS-2023-00241757. G.T. is forever grateful for the support and wisdom of his Babuji, whose recent passing has left a lasting impact on his life.

References

- [1] LUX collaboration, D. S. Akerib et al., *Results of a Search for Sub-GeV Dark Matter Using 2013*

- LUX Data*, *Phys. Rev. Lett.* **122** (2019) 131301, [[1811.11241](#)].
- [2] SENSEI collaboration, L. Barak et al., *SENSEI: Direct-Detection Results on sub-GeV Dark Matter from a New Skipper-CCD*, *Phys. Rev. Lett.* **125** (2020) 171802, [[2004.11378](#)].
- [3] EDELWEISS collaboration, Q. Arnaud et al., *First germanium-based constraints on sub-MeV Dark Matter with the EDELWEISS experiment*, *Phys. Rev. Lett.* **125** (2020) 141301, [[2003.01046](#)].
- [4] PANDAX collaboration, D. Zhang et al., *Search for Light Fermionic Dark Matter Absorption on Electrons in PandaX-4T*, *Phys. Rev. Lett.* **129** (2022) 161804, [[2206.02339](#)].
- [5] DAMIC collaboration, A. Aguilar-Arevalo et al., *Constraints on Light Dark Matter Particles Interacting with Electrons from DAMIC at SNOLAB*, *Phys. Rev. Lett.* **123** (2019) 181802, [[1907.12628](#)].
- [6] R. Essig, J. Mardon and T. Volansky, *Direct Detection of Sub-GeV Dark Matter*, *Phys. Rev. D* **85** (2012) 076007, [[1108.5383](#)].
- [7] M. J. Dolan, F. Kahlhoefer and C. McCabe, *Directly detecting sub-GeV dark matter with electrons from nuclear scattering*, *Phys. Rev. Lett.* **121** (2018) 101801, [[1711.09906](#)].
- [8] J. D. Vergados and H. Ejiri, *The role of ionization electrons in direct neutralino detection*, *Phys. Lett. B* **606** (2005) 313–322, [[hep-ph/0401151](#)].
- [9] C. C. Moustakidis, J. D. Vergados and H. Ejiri, *Direct dark matter detection by observing electrons produced in neutralino-nucleus collisions*, *Nucl. Phys. B* **727** (2005) 406–420, [[hep-ph/0507123](#)].
- [10] N. F. Bell, J. B. Dent, J. L. Newstead, S. Sabharwal and T. J. Weiler, *Migdal effect and photon bremsstrahlung in effective field theories of dark matter direct detection and coherent elastic neutrino-nucleus scattering*, *Phys. Rev. D* **101** (2020) 015012, [[1905.00046](#)].
- [11] G. Grilli di Cortona, A. Messina and S. Piacentini, *Migdal effect and photon Bremsstrahlung: improving the sensitivity to light dark matter of liquid argon experiments*, *JHEP* **11** (2020) 034, [[2006.02453](#)].
- [12] W. Wang, K.-Y. Wu, L. Wu and B. Zhu, *Direct detection of spin-dependent sub-GeV dark matter via Migdal effect*, *Nucl. Phys. B* **983** (2022) 115907, [[2112.06492](#)].
- [13] N. F. Bell, J. B. Dent, R. F. Lang, J. L. Newstead and A. C. Ritter, *Observing the Migdal effect from nuclear recoils of neutral particles with liquid xenon and argon detectors*, *Phys. Rev. D* **105** (2022) 096015, [[2112.08514](#)].
- [14] CDEX collaboration, Z. Y. Zhang et al., *Constraints on Sub-GeV Dark Matter–Electron Scattering from the CDEX-10 Experiment*, *Phys. Rev. Lett.* **129** (2022) 221301, [[2206.04128](#)].
- [15] M. Ibe, W. Nakano, Y. Shoji and K. Suzuki, *Migdal Effect in Dark Matter Direct Detection Experiments*, *JHEP* **03** (2018) 194, [[1707.07258](#)].
- [16] K. V. Berghaus, A. Esposito, R. Essig and M. Sholapurkar, *The Migdal effect in semiconductors for dark matter with masses below ~ 100 MeV*, *JHEP* **01** (2023) 023, [[2210.06490](#)].
- [17] D. Adams, D. Baxter, H. Day, R. Essig and Y. Kahn, *Measuring the Migdal effect in semiconductors for dark matter detection*, *Phys. Rev. D* **107** (2023) L041303, [[2210.04917](#)].
- [18] A. Migdal, *Ionization of atoms accompanying α - and β - decay*, *J. Phys. USSR* **4** (1941) 449.
- [19] R. Essig, J. Pradler, M. Sholapurkar and T.-T. Yu, *Relation between the Migdal Effect and Dark Matter–Electron Scattering in Isolated Atoms and Semiconductors*, *Phys. Rev. Lett.* **124** (2020) 021801, [[1908.10881](#)].

- [20] D. Baxter, Y. Kahn and G. Krnjaic, *Electron Ionization via Dark Matter-Electron Scattering and the Migdal Effect*, *Phys. Rev. D* **101** (2020) 076014, [[1908.00012](#)].
- [21] N. F. Bell, J. B. Dent, B. Dutta, S. Ghosh, J. Kumar and J. L. Newstead, *Low-mass inelastic dark matter direct detection via the Migdal effect*, *Phys. Rev. D* **104** (2021) 076013, [[2103.05890](#)].
- [22] J. Li, L. Su, L. Wu and B. Zhu, *Spin-dependent sub-GeV inelastic dark matter-electron scattering and Migdal effect. Part I. Velocity independent operator*, *JCAP* **04** (2023) 020, [[2210.15474](#)].
- [23] D. Tucker-Smith and N. Weiner, *Inelastic dark matter*, *Phys. Rev.* **D64** (2001) 043502, [[hep-ph/0101138](#)].
- [24] P. W. Graham, R. Harnik, S. Rajendran and P. Saraswat, *Exothermic Dark Matter*, *Phys. Rev. D* **82** (2010) 063512, [[1004.0937](#)].
- [25] A. L. Fitzpatrick, W. Haxton, E. Katz, N. Lubbers and Y. Xu, *The Effective Field Theory of Dark Matter Direct Detection*, *JCAP* **1302** (2013) 004, [[1203.3542](#)].
- [26] N. Anand, A. L. Fitzpatrick and W. C. Haxton, *Weakly interacting massive particle-nucleus elastic scattering response*, *Phys. Rev.* **C89** (2014) 065501, [[1308.6288](#)].
- [27] XENON collaboration, E. Aprile et al., *Search for Light Dark Matter Interactions Enhanced by the Migdal Effect or Bremsstrahlung in XENON1T*, *Phys. Rev. Lett.* **123** (2019) 241803, [[1907.12771](#)].
- [28] DARKSIDE collaboration, P. Agnes et al., *Search for Dark-Matter–Nucleon Interactions via Migdal Effect with DarkSide-50*, *Phys. Rev. Lett.* **130** (2023) 101001, [[2207.11967](#)].
- [29] SUPERCDMS collaboration, M. F. Albakry et al., *Search for low-mass dark matter via bremsstrahlung radiation and the Migdal effect in SuperCDMS*, *Phys. Rev. D* **107** (2023) 112013, [[2302.09115](#)].
- [30] G. Tomar, S. Kang and S. Scopel, *Low-mass extension of direct detection bounds on WIMP-quark and WIMP-gluon effective interactions using the Migdal effect*, *Astropart. Phys.* **150** (2023) 102851, [[2210.00199](#)].
- [31] P. Cox, M. J. Dolan, C. McCabe and H. M. Quiney, *Precise predictions and new insights for atomic ionization from the Migdal effect*, *Phys. Rev. D* **107** (2023) 035032, [[2208.12222](#)].
- [32] P. Gondolo, S. Kang, S. Scopel and G. Tomar, *Effective theory of nuclear scattering for a WIMP of arbitrary spin*, *Phys. Rev. D* **104** (2021) 063017, [[2008.05120](#)].
- [33] S. Kang, S. Scopel, G. Tomar and J.-H. Yoon, *Present and projected sensitivities of Dark Matter direct detection experiments to effective WIMP-nucleus couplings*, *Astropart. Phys.* **109** (2019) 50–68, [[1805.06113](#)].
- [34] I. Jeong, S. Kang, S. Scopel and G. Tomar, *WimPyDD: An object-oriented Python code for the calculation of WIMP direct detection signals*, *Comput. Phys. Commun.* **276** (2022) 108342, [[2106.06207](#)].
- [35] R. Catena and B. Schwabe, *Form factors for dark matter capture by the Sun in effective theories*, *JCAP* **1504** (2015) 042, [[1501.03729](#)].
- [36] S. Knapen, J. Kozaczuk and T. Lin, *Migdal Effect in Semiconductors*, *Phys. Rev. Lett.* **127** (2021) 081805, [[2011.09496](#)].
- [37] D. Bowman, C. Lim and R. Aziz, *Velocity of sound in liquid argon at high pressures and temperatures*, *Canadian Journal of Chemistry* **46** (1968) 1175–1180.
- [38] SUPERCDMS collaboration, R. Agnese et al., *Search for Low-Mass Dark Matter with CDMSlite Using a Profile Likelihood Fit*, *Phys. Rev. D* **99** (2019) 062001, [[1808.09098](#)].

- [39] XENON collaboration, E. Aprile et al., *Dark Matter Search Results from a One Ton-Year Exposure of XENON1T*, *Phys. Rev. Lett.* **121** (2018) 111302, [[1805.12562](#)].
- [40] PICO collaboration, C. Amole et al., *Dark Matter Search Results from the PICO-60 C₃F₈ Bubble Chamber*, *Phys. Rev. Lett.* **118** (2017) 251301, [[1702.07666](#)].
- [41] PICO collaboration, C. Amole et al., *Dark Matter Search Results from the PICO-60 CF₃I Bubble Chamber*, *Submitted to: Phys. Rev. D* (2015) , [[1510.07754](#)].
- [42] DARKSIDE collaboration, P. Agnes et al., *Low-Mass Dark Matter Search with the DarkSide-50 Experiment*, *Phys. Rev. Lett.* **121** (2018) 081307, [[1802.06994](#)].
- [43] LZ collaboration, J. Aalbers et al., *First Dark Matter Search Results from the LUX-ZEPLIN (LZ) Experiment*, *Phys. Rev. Lett.* **131** (2023) 041002, [[2207.03764](#)].
- [44] CDEX collaboration, L. T. Yang et al., *Limits on light WIMPs with a 1 kg-scale germanium detector at 160 eVee physics threshold at the China Jinping Underground Laboratory*, *Chin. Phys.* **C42** (2018) 023002, [[1710.06650](#)].
- [45] SUPERCDMS collaboration, R. Agnese et al., *Low-mass dark matter search with CDMSlite*, *Phys. Rev.* **D97** (2018) 022002, [[1707.01632](#)].
- [46] G. Adhikari et al., *An experiment to search for dark-matter interactions using sodium iodide detectors*, *Nature* **564** (2018) 83–86, [[1906.01791](#)].
- [47] COUPP collaboration, E. Behnke et al., *First Dark Matter Search Results from a 4-kg CF₃I Bubble Chamber Operated in a Deep Underground Site*, *Phys. Rev.* **D86** (2012) 052001, [[1204.3094](#)].
- [48] CRESST collaboration, G. Angloher et al., *Results on light dark matter particles with a low-threshold CRESST-II detector*, *Eur. Phys. J.* **C76** (2016) 25, [[1509.01515](#)].
- [49] PANDAX-II collaboration, X. Cui et al., *Dark Matter Results From 54-Ton-Day Exposure of PandaX-II Experiment*, *Phys. Rev. Lett.* **119** (2017) 181302, [[1708.06917](#)].
- [50] E. Behnke et al., *Final Results of the PICASSO Dark Matter Search Experiment*, *Astropart. Phys.* **90** (2017) 85–92, [[1611.01499](#)].
- [51] SUPERCDMS collaboration, R. Agnese et al., *Results from the Super Cryogenic Dark Matter Search Experiment at Soudan*, *Phys. Rev. Lett.* **120** (2018) 061802, [[1708.08869](#)].
- [52] XENON collaboration, E. Aprile et al., *First Dark Matter Search with Nuclear Recoils from the XENONnT Experiment*, *Phys. Rev. Lett.* **131** (2023) 041003, [[2303.14729](#)].